High-resolution quantification of metabolic heat output from individual live Drosophila brains

Kanishka Panda[1], Rohith Mittapally[1], Qianqian Chen[2], Akshay Bhaskaran[1], Pramod Reddy[1,3,4]*, Edgar Meyhofer[1,5]*, Swathi Yadlapalli[2]*

[1]Department of Mechanical Engineering, University of Michigan, Ann Arbor, MI, USA.

[2]Cell and Developmental Biology, University of Michigan, Ann Arbor, MI, USA.

[3]Department of Electrical Engineering and Computer Science, University of Michigan, Ann Arbor, MI, USA.

[4]Department of Materials Science and Engineering, University of Michigan, Ann Arbor, MI, USA.

[5]Department of Biomedical Engineering, University of Michigan, Ann Arbor, MI, USA.

*Correspondence: pramodr@umich.edu, meyhofer@umich.edu, swathi@umich.edu

Abstract

Quantitative insights into brain metabolism are essential for advancing our understanding of the energy dynamics in the brain. However, current approaches to tracking brain metabolism, such as metabolic profiling, offer only static snapshots of metabolite levels and fall short in capturing real-time energy fluxes. Here, we present the first direct, quantitative measurement of metabolic output from individual, live explanted brains of *Drosophila melanogaster* using a high-resolution biocalorimeter capable of detecting nanowatt-scale metabolic changes, while maintaining brain viability *via* continuous buffer perfusion. Using this platform, we measured an average metabolic output of ~256 nW per brain in female, 10-day-old *Drosophila* flies. Notably, female brains exhibited significantly higher metabolic activity than male brains at a young age (10-day-old). Furthermore, in *parkin* mutants—used to model Parkinson's disease—homozygous mutant brains showed a ~15% reduction in metabolic output relative to heterozygous controls, consistent with impaired mitochondrial function. We further extended our measurements to other *Drosophila* tissues, demonstrating that mass-normalized metabolic rates of ovaries and testes are ~2.5-fold lower compared to brains in *Drosophila*, highlighting the brain's exceptional energy demands. This platform enables real-time, quantitative brain bioenergetics studies and is adaptable to tissue organoids and drug screening, offering new avenues for investigating aging, neurodegeneration, and metabolism-driven disease mechanisms.

Introduction

The adult human brain, despite comprising only 2% of body weight, consumes 20% of resting energy to drive complex behaviors like decision-making[1]. This exceptionally high energy demand renders the brain particularly vulnerable to disruptions in energy production and flow. Dysregulated brain metabolism has been implicated in numerous neurodegenerative diseases, including Alzheimer's[2], Parkinson's[3], as well as age-related cognitive decline[4, 5]. Understanding the energy dynamics in the brain is critical for developing therapeutic interventions. However, current tools for studying cellular bioenergetics in live, intact brains—particularly in model organisms—remain limited.

Current approaches for investigating brain metabolism, such as metabolic profiling[6-11], and respirometry[12, 13], each have critical drawbacks. Techniques like metabolic profiling provide only static snapshots of metabolite levels, fail to capture real-time energy fluxes, and typically require destructive sample preparation, precluding long-term metabolic measurements. Respirometry, while being effective in assessing whole-organism oxygen consumption[12, 13], lacks the sensitivity required for small-tissues and is generally restricted to large cell populations or isolated mitochondria[14]. As a result, there is a critical need for employing new tools capable of non-invasive quantification of real-time metabolic activity in live brain tissue under physiological and pathophysiological conditions.

Direct calorimetry overcomes the above challenges by measuring metabolic heat output[15, 16]—a universal byproduct of cellular energy transduction[17, 18]—providing a label-free, integrative view of total energy flux. Recent advances in biocalorimetry have enabled nanowatt-scale heat detection, making it possible to study dynamic metabolic processes during early embryonic

development[19-22], detect age-related metabolic decline in model organisms such as *Drosophila melanogaster*[23] and *C. elegans*[24], and measure heat output from single *Tetrahymena thermophila* cells[25]. Despite these technical breakthroughs, implementing direct calorimetry to individual, live explanted tissues such as brains remains challenging, as it requires both sustained tissue viability and high sensitivity.

Brain explant cultures offer a powerful model system for studying neural activity, development, and disease in a controlled yet physiologically relevant context[26, 27]. In these preparations, neural tissues are carefully dissected and maintained *ex vivo* in specialized media that preserve their complex cellular architecture and organotypic properties. Brain explants are widely used across species—for instance, rodent hippocampal slices to investigate learning and memory[26], and adult retinal explants for neural development and axon guidance[27]. These explant models provide a critical bridge between *in vivo* experiments and dissociated cell cultures, which makes them ideally suited for probing tissue-level bioenergetics, but their small size and fragility demand highly sensitive, non-invasive tools for real-time metabolic assessment. To date, direct measurements of metabolic heat in live brain explants have remained elusive.

Here, we present a high-resolution biocalorimeter with nanowatt sensitivity and ~40 s response time while preserving tissue viability via continuous buffer perfusion (~4 µl/min) that enables, for the first time, direct, real-time measurements of metabolic output from individual, live explanted *Drosophila melanogaster* brains. We validated this technique using mitochondrial inhibitors, which suppressed brain metabolism by 25–80%. Using this platform, we uncovered sex-, genotype-, age-, and disease-dependent differences in brain metabolism. We discovered that young female brains showed significantly higher metabolic output than males, a difference

that diminished with age. In *parkin* mutants modeling Parkinson's disease, homozygous brains exhibited ~15% reduced metabolic output relative to heterozygotes. Extending the method to reproductive tissues, we found metabolic output from individual ovaries and testes to be ~2.5-fold lower than that of the brain, highlighting the brain's high energy demands. This approach provides a powerful tool for real-time metabolic assessment in small, intact brains of model organisms, enabling new insights into brain energetics, aging, and disease. Beyond brains, this method can be extended to tissue organoids and drug screening platforms, broadening its impact on studies of metabolism, therapeutic development, and age-related disorders.

Results

High-resolution biocalorimeter

We present a highly sensitive calorimeter capable of measuring nanowatt-level heat power changes, adapted for measuring the metabolic outputs of *Drosophila* brains using a continuously flowing physiological buffer to maintain the explanted brains alive. The calorimeter comprises of a vacuum-suspended, capillary-based sensor, i.e. sensing capillary that is housed within two nested shields (Fig. 1a), which along with μTorr levels of vacuum, precision temperature sensing and PID-based active temperature control, help maintain a high temperature stability in the calorimeter. The sensing capillary (Fig. 1b) consists of a cylindrical tube made of Teflon Perfluoroalkoxy resin (PFA), used for its inertness and low thermal conductivity[28]. The capillary's dimensions (750 μm inner and 1 mm outer diameter) are selected to accommodate brains of *Drosophila* fruit flies, with sizes up to ~750 μm[29] along their largest dimension. A precision thermistor is mounted at the center along the length of the capillary, and acts as a thermometric sensor for detecting temperature changes caused by metabolic heat outputs from explanted *Drosophila* brains. The sensing capillary is suspended across the open side of the inner

shield (IS) (see Methods). The anchor points of the capillary (i.e., ends of the suspended part of the capillary tube) are in excellent thermal contact with the IS, which is stabilized to be within ±1 μK of the set point (~295 K) over 10 hours, as shown in our past work[30]. The sensing capillary further extends out of the two shields and is connected to a syringe pump and a reservoir (Fig. 1a), necessary for loading and unloading brain samples and maintaining continuous flow of a buffer solution during metabolic measurements. A stopper is inserted from one end of the capillary to locate the brain near the thermistor. The stopper is made of an optical glass fiber that also acts as a light source for imaging the sample, together with optical windows assembled on the outer shield (OS) and an inverted optical microscope (Zeiss Axiovert 200 with a 10X objective). An identical matching capillary (Fig. 1a) is mounted close to the sensing capillary to enable common-mode cancellation of background thermal drifts, helping enhance the heat power resolution by improving the stability of the temperature signal[30]. The fabrication and assembly of the calorimeter is described further in Methods and in Supplementary Fig. S1.

Continuous flow of a physiological buffer solution is necessary for supplying nutrients and oxygen to the explanted brain and maintaining it alive during the calorimetric measurements. We used a buffer made of Schneider's Drosophila medium supplemented with 1% Antibiotic-Antimycotic solution (Invitrogen), 10% fetal bovine serum (FBS), and 10 μg/ml insulin. The optimum buffer flow rate for the metabolic activity measurements of *Drosophila* brains was found to be 4 μl/min (explained further in the next section). The key calorimetric parameters, i.e. temperature resolution, thermal conductance, and time constant of the sensing capillary were characterized as ~30 μK (ΔT), ~255 μW/K (G_{th}) and ~40 seconds, respectively, with a 4 μl/min buffer flow (Supplementary Fig. S2). The heat output from the brain can be estimated[31] from the

temperature change near the sensor, given by $\dot{Q} = G_{th} \times \Delta T$. The heat power resolution of the calorimeter was hence determined as ~7.6 nW with a buffer flow of 4 µl/min.

Quantification of metabolic activity in *Drosophila* brains

To measure the metabolic heat output from individual fly brains, the flies were synchronized to a 12-hour light/12-hour dark cycle and maintained in an incubator at a constant temperature of 25°C and 50% relative humidity for a minimum of 3 days prior to measurements. Experiments were started two hours after light onset to ensure consistent metabolic activity comparisons across various conditions. We started by testing whether we can precisely measure the metabolic heat output of an individual *Drosophila* brain, following the method depicted in Fig. 1b. We dissected a brain using the buffer described earlier, that preserves the health and metabolic activity of dissected tissues for extended periods[32, 33]. After dissection, we transferred the brain into the calorimeter's reservoir and subsequently loaded it into the sensing capillary using the fluid flow generated with a syringe pump. The brain was held near the sensing thermistor by the stopper and an opposing fluid flow. The buffer flow was then set to the desired continuous flow rate (4 µl/min), after which the calorimeter needed ~20 minutes for thermal stabilization before beginning the measurement. The measurement was performed for ~1 hour after loading the brain, and then the brain was unloaded. The temperature changes at the thermistors on the sensing and the matching capillaries were measured using two independent Wheatstone bridge circuits and lock-in amplifiers (SR830, Stanford Research Systems) and the temperature rise caused by the metabolism of the brain was determined as a differential signal between the sensing and the matching capillary sensors to eliminate the common-mode thermal drift. The instrumentation and the measurement scheme are further described in Methods and in Supplementary Fig. S4b. The metabolic heat output of the brain was estimated from:

$\dot{Q}_{\text{metabolic}} = G_{\text{th}} \times \Delta T_{\text{metabolic}}$. Fig. 1c plots the trace of a complete metabolic rate measurement from the brain of an individual, 10-day-old female fly (*y sc v* genotype), whose metabolic heat output was measured to be ~250 nW. This trace also shows that the temperature signal remains stable for at least ~1 hour of continuous measurement with the brain loaded in the calorimeter.

Upon performing measurements on 8 similar brains with a buffer flow rate of 4 µl/min, the average metabolic output per brain in 10-day-old female flies (*y sc v* genotype) was measured to be ~256 nW. To investigate the effect of buffer flow rate on the observed metabolic outputs, we repeated these measurements at buffer flow rates of 2 µl/min and 6 µl/min. Fig. 1d plots the averaged traces of the metabolic output measured for 6-8 female brains each with 2, 4 and 6 µl/min buffer flow rates. For a flow rate of 2 µl/min, we observed a very low heat output (~62 nW), that was not stable and gradually kept reducing over time, which we believe was due to an insufficient supply of nutrients or oxygen to the brains. We observed a stable mean metabolic output of ~247 nW at a flow rate of 6 µl/min, indistinguishable from the output at 4 µl/min. We also determined the mass-normalized metabolic rate by estimating the dry mass of each brain, following the procedure explained in Methods and in Supplementary Fig. S6-S7. The distribution of the absolute and normalized metabolic rates at the three flow rates (2, 4 and 6 µl/min) are shown in Supplementary Fig. S5a and S5b, respectively. This flow dependency study confirms that a continuous flow of the buffer at 4 µl/min is sufficient to maintain a *Drosophila* brain metabolically active, and all following measurements are performed at the flow rate of 4 µl/min.

Validation of the metabolic activity measurements

Previous studies using respirometry have demonstrated that cellular metabolism responds dynamically to environmental and pharmacological stimuli, including changes in oxygen availability[34], or exposure to mitochondrial inhibitors[35]. To test whether the metabolic heat

output of brains is reduced upon exposure to mitochondrial inhibitors, we investigated the effects of disrupting the electron transport chain (ETC) and oxidative phosphorylation on metabolic activity. Specifically, we used rotenone, a complex I inhibitor that blocks electron transfer from NADH to ubiquinone, thus reducing ATP production, and antimycin, a complex III inhibitor that prevents electron transfer from ubiquinol to cytochrome c, thereby decreasing ATP synthesis and altering mitochondrial respiration[36].

We measured the absolute and normalized metabolic rates of the brains without inhibitor, with rotenone (0.5 μM) and with antimycin (0.5 μM and 20 μM). For these experiments, we incubated *Drosophila* brains in buffer with desired concentrations of rotenone and antimycin for an additional one hour after dissection and before loading into the calorimeter for measurement, to acclimatize the brains to the inhibitors (Fig. 2a). For a fair comparison with the experiments performed without inhibitor, the brains were also incubated for one hour in the control buffer. The metabolic output of brains incubated in control buffer for one hour remained consistent with the outputs measured in the same buffer without a one-hour incubation, showing no significant differences (Fig. 2b). However, exposure to 0.5 μM antimycin resulted in a ~25% decrease in the metabolic heat output, while 20 μM antimycin led to a ~80% decrease compared to the control. Similarly, exposure to 0.5 μM rotenone resulted in a ~60% decrease in the metabolic output. The averaged traces and the distribution of the absolute metabolic rates are plotted in Fig. 2c and 2d, respectively. Further, we observed that normalized metabolic rates of brains exposed to antimycin or rotenone were also significantly lower than those of the controls (Fig. 2e). These results, demonstrating reduced metabolic heat output following mitochondrial inhibitor treatment, are consistent with our expectations based on the known effects of mitochondrial inhibitors on ATP synthesis. These results validate our calorimetric method's capability to

precisely measure the changes in metabolic activity in individual brains in response to various stimulus.

Next, we performed measurements to investigate metabolic variations in *Drosophila* brains associated with gender, genotype, age, and diseases. For these studies, we followed the protocol depicted in Fig. 1b, where the brain is dissected, imaged for size/mass estimation, and directly loaded into the calorimeter with the buffer medium for metabolic output measurement.

Quantification of metabolic activity in fly brains across different genders and genotypes

First, we investigated how the metabolism of *Drosophila* brains varies with gender and genotype, with the observations plotted in Fig. 3. Interestingly, we observed that the brain's metabolic heat output in young (10-day-old) female flies is significantly higher than that in young male flies in both *y sc v* and the w^{1118} genotypes. Although female brains are slightly larger and have a higher dry mass, the metabolic heat output, when normalized for dry mass remains significantly higher in females than in males. We also observed that brains from the *y sc v* genotype exhibit higher metabolic heat output compared to those from the w^{1118} genotype across both genders. However, these differences disappeared when the metabolic heat outputs were normalized to their dry mass, since brains from the *y sc v* genotype are larger than those from the w^{1118} genotype.

In conclusion, our findings indicate that normalized metabolic activity in young female brains is significantly higher than in males across different genotypes, although the underlying mechanisms remain to be elucidated. Overall, these results provide novel insights into the metabolic dynamics of *Drosophila* brains, highlighting the potential for further studies on metabolic variation due to genetic and physiological factors.

Quantification of metabolic activity in fly brains across lifespan

Understanding how metabolic activity in specific organs, such as the brain, changes over the lifespan is crucial due to its potential contributions to age-related diseases. Aging is intimately linked with neurodegenerative disorders[5], underscoring the importance of studying how brain metabolism evolves with age. We explored age-related changes in metabolic activity of *Drosophila* brains across genders and these findings are shown in Fig. 4. Intriguingly, we discovered that female brains exhibit a higher metabolic output at a younger age, which gradually declines over their lifespan. Specifically, we observed that female brain metabolic activity decreases from day-10 to day-30, then either stabilizes or slightly increases until day-45, depending on the genotype. Additionally, when we quantified normalized metabolic activity, it was significantly higher in younger flies (day-10) across all genotypes compared to their older counterparts at day-30 or day-45. This pattern underscores the dynamic nature of metabolic changes over the lifespan of female *Drosophila* flies. In contrast, male brains displayed relatively stable metabolic activity throughout their lifespan from day-10 to day-45, for both *y sc v* and w^{1118} genotypes. Our use of this calorimetric method has enabled us to document the variations in brain metabolic aging for the first time, revealing distinct metabolic trajectories in male and female brains over their lifespan.

Quantification of metabolic activity in mitochondrial mutant fly brains

We next explored how mutations in mitochondrial genes such as Parkin, which are linked to Parkinson's disease, affect the metabolic activity in brains. Parkin, encoded by the PARK2 gene, is vital for maintaining cellular health by regulating mitochondrial function. Parkin functions as an E3 ubiquitin ligase, tagging damaged mitochondria for degradation via the mitophagy pathway[37, 38], thus preventing the accumulation of dysfunctional mitochondria that can lead to cellular stress and apoptosis. Mutations in Parkin disrupt this critical process, leading to an

accumulation of defective mitochondria. This results in impaired cellular energy production, increased oxidative stress, and the release of pro-apoptotic factors. Parkin null *Drosophila* display Parkinsonian-like phenotypes, including reduced life span, climbing and flying disability, sterility, mitochondrial defects and dopaminergic neurodegeneration[39].

In our study (Fig. 5), we assessed the impact of Parkin-mediated mitochondrial dysfunction on brain metabolic activity using *Drosophila* models heterozygous or homozygous for the Parkin mutation. We observed that brains from heterozygous mutants ($park^1$/+) exhibited a metabolic output of ~246 nW, whereas brains from homozygous mutants ($park^1$) showed ~211 nW, i.e., a ~15% reduction in output. Importantly, these differences in metabolic outputs were also evident when normalized for brain dry mass.

Quantification of metabolic activity in other *Drosophila* tissues

Finally, we performed measurements quantifying metabolic activity in other *Drosophila* tissues like ovaries and testes, demonstrating the general capabilities of the developed calorimetric method. In these studies, we followed similar dissection, loading, and measurement protocols as described in Fig. 1. Supplementary Fig. S8a and S8b show one representative measurement trace each for an individual ovary and an individual testis, respectively. Measurements performed on 6 ovaries and 6 testes revealed an average metabolic heat output of ~132 nW per ovary and ~83 nW per testis, in 10-day-old flies of the *y sc v* genotype (Fig. 6a-b).

For a direct comparison of the normalized metabolic rates of these tissues, we measured their dry masses using an ultra-microbalance (see Methods and Supplementary Fig. S7a). The mean dry masses of female brains, ovaries, and testes were found to be ~6.6 µg, ~9.2 µg, and ~5.2 µg, respectively (Supplementary Fig. S7b). Thus, we estimated the normalized metabolic outputs to be ~38.7 nW/µg for female brains, ~14.4 nW/µg for ovaries, and ~15.9 nW/µg for

testes, in 10-day-old flies of the *y sc v* genotype (Fig. 6c). Our observations suggest that the brain's normalized metabolic activity is significantly (~2.5 fold) higher than that of ovaries and testes, supporting the idea that the brain is one of the most energy-consuming organs in *Drosophila* flies. Our demonstrations underscore the versatility and efficacy of this calorimetric method in providing detailed metabolic insights across different tissues in addition to brains, establishing it as a powerful tool for metabolic studies in a range of small biological tissues.

Discussion

We present a biocalorimetry method that enables, for the first time, direct, real-time measurements of metabolic output from small neural tissues, such as live explanted *Drosophila melanogaster* brains. The biocalorimeter can detect heat power changes as small as ~7.6 nW with a response time of ~40 seconds, while preserving brain viability via continuous buffer perfusion (~4 µl/min), enabling stable metabolic measurements on individual explanted brains for over 1 hour. We performed experiments to confirm the biocalorimeter's sensitivity in detecting metabolic shifts. Exposure to mitochondrial inhibitors (0.5 µM antimycin: ~25% reduction; 20 µM antimycin: ~80% reduction; 0.5 µM rotenone: ~60% reduction) reduced brain metabolic activity, consistent with their known disruption of ATP synthesis via the electron transport chain. This validates our method as a robust tool for studying dynamic metabolic responses to pharmacological and environmental stimuli in individual, intact brains.

Our quantification of metabolic activity across genders and genotypes uncovered novel insights. Female *Drosophila* brains exhibited significantly higher metabolic rates than male brains for both *y sc v* and w^{1118} genotypes even when normalized for dry mass. This disparity in metabolic output cannot be solely attributed to the cell numbers between genders, as recent

studies have not shown significant differences in the cell numbers between male and female *Drosophila* brains[40]. Potential factors that could contribute to higher metabolic rates in female brains include increased neuronal activity, hormonal influences on metabolism, or genetic variations affecting metabolic pathways. Age-related analyses revealed distinct metabolic trajectories: female brains showed a sharp decline in metabolic rate from day-10 to day-30, which stabilized or slightly increased by day-45, while male brains remained stable throughout day-10 to day-45. These gender-specific patterns, previously unreported, highlight the capability to track metabolic aging in brains, providing insights into the metabolic basis of age-related diseases.

In *Drosophila* models of Parkinson's disease[39], homozygous mutants (*park*^{1}) exhibited a ~15% reduction in brain metabolic output (~211 nW) compared to heterozygous mutants (*park*^{1}/+, ~246 nW), even after dry mass normalization. These findings align with Parkin's role in mitophagy suggesting that mitochondrial dysfunction impairs energy production, contributing to neuronal stress. This highlights the potential of our calorimetric method for studying disease-relevant metabolic alterations in brains, offering a novel approach for investigating neurodegenerative mechanisms.

Finally, we demonstrated the capability to quantify metabolic outputs in other tissues of *Drosophila* beyond brains, such as reproductive organs like ovaries and testes. We reported metabolic outputs of ~132 nW and ~83 nW in ovaries and testes of 10-day-old *Drosophila*, compared to the output of ~256 nW in brains of female 10-day-old *Drosophila*. Notably, the brain's normalized metabolic rate (~38.7 nW/μg) was ~2.5-fold higher compared to ovaries

(~14.4 nW/μg) and testes (~15.9 nW/μg), supporting the notion that brain is a highly energy-intensive organ.

In conclusion, the presented calorimetric technique represents a transformative tool for bioenergetics, enabling precise, real-time metabolic measurements in individual, intact brains of small model organisms like *Drosophila*, providing new insights into brain energetics, aging, and disease. Using this platform, we discovered novel sex-, age-, genotype-, and disease-dependent patterns in brain metabolism. By bridging the gap in quantitative bioenergetics, our studies open new avenues for understanding cellular energy dynamics in health and disease. Beyond brains, this method can be extended to tissue organoids and drug screening platforms, broadening its impact on studies of metabolism, therapeutic development, and age-related disorders.

Methods

Calorimeter fabrication and assembly

Two cylindrical capillary tubes (0.75 mm and 1 mm inner and outer diameters, respectively) made of Teflon PFA are prepared as the sensing and the matching capillary sensors (Fig. 1a). The process for the fabrication and assembly of the sensing capillary is shown by Steps 1-7 in Supplementary Fig. S1. The PFA capillary is cleaned with acetone and iso-propyl alcohol to prepare for metal deposition (Step 1). A 5/100 nm-thin titanium/gold film is deposited using e-beam evaporation throughout the cylindrical surface of the capillary except at a small window at the center (Step 2). This window electrically isolates the metal on the two sides of the capillary and also allows for optical access. A miniature thermistor (Ametherm, NTC, SM06103395) with 10 kΩ nominal resistance at 25°C is used as the thermometric sensor for metabolic measurements. The thermistor is mounted at the center along the length of the capillary, soldered to the isolated gold layers on either side such that the gold extends the electrical connection from the two terminals of the thermistor to the external electrical instrumentation (Step 3).

The outer shield (OS, 12×12×8 cm^3) is designed to be a vacuum enclosure while the inner shield (IS, 7×7×3.5 cm^3) is U-shaped and is enclosed on 5 sides but open on one side, and both shields are made of copper. The sensing capillary with the mounted thermistor is assembled onto the IS, such that ~20 mm length of the capillary is suspended between two anchor regions on the open-side of the IS (Step 4). 50 μm-thin glass sheets are placed at the anchor regions on the IS, and the capillary is mounted on the glass using a thermally conductive silver epoxy. The glass helps electrically isolate the gold on the capillary from the copper body of the IS. A small copper lid (part of the IS), with a cylindrical groove of 1 mm diameter and lined with a thin, soft graphite sheet, encloses the capillary from the top side and is mechanically screwed down to the

rest of the IS. The graphite fills the air pockets between the capillary and the groove of the copper lid, and ensures that the capillary is in excellent thermal contact with the IS. The IS is housed inside the OS (Step 5), and the sensing capillary extends out of the OS through hermetically sealed PEEK feedthroughs and connectors (Idex MicroTight series). A multimode optical fiber (Thor Labs, UM22-300, 370 μm outer diameter) is inserted into the capillary from one side and extends till the center of the suspended length of the capillary (Step 6). It acts as a stopper to localize biological samples near the thermistor for metabolic measurements and also acts as a light source for optical imaging of the samples. One end of the capillary (same end through which the stopper is inserted) is connected to a syringe pump, while the other end of the capillary sinks in a reservoir, which together completes a microfluidic system. A physiological buffer is then filled into the capillary for biocalorimetry measurements (Step 7).

The primary difference between the sensing and matching capillaries is that the latter does not extend out of the OS, does not have a stopper, and is not filled with buffer. The process for the fabrication and assembly of the matching capillary follows Steps 1-4 shown in Supplementary Fig. S1, i.e. it is identical to the process for the sensing capillary till after its assembly with the IS.

Temperature stabilization

A nested two-shield system is designed to isolate the sensing and matching capillaries from the ambient temperature fluctuations. Some aspects of the calorimeter design and the temperature stabilization techniques are carried forward from our past work[24, 30] but are described here for completeness. OS and IS are made of highly thermally conductive copper, have large masses to dampen the high-frequency temperature oscillations, and are isolated from each other using weak thermal links. Fig. 1a shows the nested two-shield design, where the IS is mounted inside the OS

using four borosilicate spheres sitting on conical grooves machined at the base of the OS, connecting the two shields conductively at approximate line contacts. Vacuum conditions < 10 μTorr are maintained inside the OS, which is known to significantly attenuate the convective heat transfer coefficient[41]. Radiative heat transfer between the shields is further reduced by using reflective aluminum sheets (emissivity < 0.07[28]) on the shield surfaces. Finally, the OS is externally enclosed with reflective foam insulation to prevent air currents from perturbing the system.

High-precision temperature sensing and active PID-based temperature control is employed to eliminate low-frequency (long-term) temperature drifts in the shields. Supplementary Fig. S4a shows the instrumentation developed for the temperature feedback control. AC-driven Wheatstone bridge circuits are used for resistance thermometry[42], with precision thermistors for temperature sensing (US Sensor Corp., USP 12838, 10 kΩ nominal resistance at 25°C, –4.4%/K *TCR* (temperature coefficient of resistance)) integrated into holes drilled in the walls of the OS and IS using epoxy (3M Scotch-Weld Adhesive 2216B/A). A temperature change in the shield leads to a change in the resistance of the thermistor, which is detected as a change in the voltage fluctuation using a sinusoidal sensing current in the Wheatstone bridge circuit. The output is amplified using an instrumentation amplifier (AD 524), measured as $V_{\mathrm{sens,shield}}$ (Eq. 1) and provided as an input to the PID control algorithm. The algorithm compares $V_{\mathrm{sens,shield}}$ to a pre-determined voltage setpoint V_{set} and outputs a feedback voltage V_{PID} in the range of –10 V to 10 V. The PID algorithm is implemented through LABVIEW and is represented by Eq. 2, where e is the error between $V_{\mathrm{sens,shield}}$ and V_{set}, K_C is the proportional gain, τ_i is the integral time, and τ_d is the derivative time[43]. K_C, τ_i, and τ_d are critical PID constants that need to be tuned for the desired functioning of the algorithm. V_{PID} is provided

as an input to a current-source circuit that uses an NPN transistor (ST Microelectronics 2ST31A) to adjust the heating current supplied to the polyimide heaters (Omega KH series) mounted on the surface of the shields. This helps control the temperature of the shields around a desired setpoint with high precision. Using the above method, we achieved a temperature stability within ±1 μK in the IS over 10 hours, measured at a 1 mHz bandwidth (~100 dB attenuation in the temperature fluctuations from the ambient to the IS). Our past work[30] shows these results and describes the stabilization method and instrumentation in greater detail.

$$\Delta V_{\text{sens,shield}} = V_{\text{in}} \times Gain \times \left(\frac{R_{\text{sens,shield}} + \Delta R_{\text{sens,shield}}}{R_{\text{upper}} + R_{\text{sens,shield}} + \Delta R_{\text{sens,shield}}} - \frac{R_{\text{lower}}}{R_{\text{upper}} + R_{\text{lower}} + R_{\text{pot}}} \right) \quad (1)$$

$$V_{\text{PID}}(\text{t}) = (K_{\text{C}} \times e) + \frac{K_{\text{C}}}{\tau_{\text{i}}} \times \left(\int_0^t e \times \text{d}t \right) + \left(K_{\text{C}} \times \tau_{\text{d}} \times \frac{\text{d}e}{\text{d}t}\right) \quad (2)$$

Thermometry to quantify metabolic heat output

During a metabolic heat output measurement, the biological sample is located near the thermistor at the center along the length of the suspended sensing capillary. The measured heat output is given by $\dot{Q} = G_{\text{th}} \times \Delta T$, where ΔT is the temperature change sensed by the thermistor in its proximity and G_{th} is the thermal conductance of the suspended structure to the ambient (i.e., the IS). The ability to measure small metabolic heat outputs relies on a high thermometric resolution and a small G_{th}. Here, we achieve high thermometric resolution implementing resistance thermometry[42] using a high *TCR* miniature thermistor, precise AC-driven Wheatstone bridge circuitry, and common-mode cancellation of thermal drift. Supplementary Fig. S4b shows the sensing capillary with the integrated thermistor connected to the electrical instrumentation. The sensing thermistor (Ametherm, NTC, SM06103395), connected to the lower right leg of the Wheatstone bridge, has a high *TCR* (-3.95%/K) and a nominal resistance of 10 kΩ (±1%) at 25°C ($R_{\text{sens cap}}$). A fixed 10 kΩ resistor (R_{lower}) is connected to the lower left leg of the bridge.

The upper right leg consists of a 40 kΩ fixed resistor (R_{upper}) while the upper left leg consists of a 40 kΩ fixed resistor (R_{upper}) along with a potentiometer (R_{pot}, 0 □ 500 Ω) for fine balancing of the bridge. All fixed resistors in the bridge are precision, ultra-low *TCR* resistors (Vishay Z201 Series Z-Foil, ±0.2 ppm/K), and the potentiometer is from Vishay Spectrol 534 series with a 20 ppm/K *TCR*. The temperature change due to the metabolic output from a sample causes a change in the DC resistance of the thermistor, which is detected using an AC sensing voltage (V_{AC}). Using a modulated sensing current helps attenuate the voltage noise introduced in the sensor circuits through 1/*f* noise sources and other DC offsets. Toward this, the bridge is excited using a 1 V peak-to-peak sinusoidal voltage (V_{AC}) at a frequency in the range of 20 □ 40 Hz (f_{AC}) using an Agilent 33120A waveform generator. The change in voltage across the thermistor on the sensing capillary is output from the Wheatstone bridge (at f_{AC}) and amplified by an AD 524 instrumentation amplifier. This voltage, i.e. $\Delta V_{sens\ cap}$ is given by Eq. 3, and is measured in a ~16 mHz bandwidth using a Lock-in mechanism (SRS 830) and recorded using a NI PCI-6014 DAQ card. $\Delta V_{sens\ cap}$ is converted to the corresponding resistance change ($\Delta R_{sens\ cap}$) and temperature change ($\Delta T_{sens\ cap}$) using Eqns. 4-5.

To improve the temperature resolution, a matching capillary is designed to implement a common-mode cancellation scheme to eliminate long-term temperature drifts. The matching capillary is identical to the sensing capillary but without a biological sample. The temperature change in the matching capillary is measured using a similar Wheatstone bridge circuit and following the same analysis as for the sensing capillary, described above. Temperature change in the matching capillary is primarily caused by ambient temperature fluctuations. The temperature change caused due to the metabolism of the biological sample is thus estimated by subtracting the temperature change in the sensing capillary ($\Delta T_{sens\ cap}$) and the temperature change in the

matching capillary ($\Delta T_{\text{mat cap}}$). The measured temperature change of the biological sample is converted to the metabolic heat output ($\dot{Q}_{\text{metabolic}}$) using the pre-calibrated G_{th} (Eq. 6).

$$\Delta V_{\text{sens cap}} = V_{\text{in}} \times Gain \times \left(\frac{R_{\text{sens cap}} + \Delta R_{\text{sens cap}}}{R_{\text{upper}} + R_{\text{sens cap}} + \Delta R_{\text{sens cap}}} - \frac{R_{\text{lower}}}{R_{\text{upper}} + R_{\text{lower}} + R_{\text{pot}}} \right) \tag{3}$$

$$\Delta R_{\text{sens cap}} = \frac{\Delta V_{\text{sens cap}}}{\frac{V_{\text{in}}}{R_{\text{upper}} + R_{\text{sens cap}}} \times \frac{R_{\text{upper}}}{R_{\text{upper}} + R_{\text{sens cap}}} \times Gain} \tag{4}$$

$$\Delta T_{\text{sens cap}} = \frac{\Delta R_{\text{sens cap}}}{R_{\text{sens cap}} \times TCR} = \frac{\Delta V_{\text{sens cap}}}{\frac{V_{\text{in}}}{R_{\text{upper}} + R_{\text{sens cap}}} \times \frac{R_{\text{upper}}}{R_{\text{upper}} + R_{\text{sens cap}}} \times Gain \times R_{\text{sens cap}} \times TCR} \tag{5}$$

$$\dot{Q}_{\text{metabolic}} = G_{\text{th}} \times \left(\Delta T_{\text{sens cap}} - \Delta T_{\text{mat cap}} \right) \tag{6}$$

Thermal conductance, heat power resolution, and time constant

Characterizing the thermal conductance of the suspended calorimeter requires applying a DC voltage offset ($V_{\text{DC, off}}$) in addition to the AC sensing voltage (V_{AC}). $V_{\text{DC,off}}$ causes a known power dissipation on the thermistor due to Joule heating, leading to a constant temperature rise that is measured using V_{AC} and the measurement scheme described in the previous section. The slope of the power dissipated to the temperature rise, corresponds to the thermal conductance (G_{th}). Supplementary Fig. S2a shows the G_{th} of the sensing capillary calorimeter, measured in the presence of a 4 µl/min buffer flow through the capillary. In this measurement, DC power was dissipated in the calorimeter from 0 – 160 nW in steps of 20 nW, and the corresponding temperature rise was measured from ~0 – 630 µK, resulting in a G_{th} of ~255 µW/K. As shown in Supplementary Fig. S3a, we also measured the G_{th} with buffer flow rates of 0 µl/min, 2 µl/min, and 6 µl/min, and found them to be ~210 µW/K, 228 µW/K, and 290 µW/K, respectively.

The thermal time constant of the calorimeter was characterized as ~40 seconds with a 4 µl/min buffer flow, measured at a ~16 mHz bandwidth (Fig. S2b), the same bandwidth as used for the metabolic heat output measurements. To measure this, power was dissipated from 0 □ 200 nW in steps of 100 nW. The time taken by the calorimeter to reach ~63.2% of its final temperature change due to the step power input, is the thermal time constant of the calorimeter.

To characterize the heat power resolution, the DC power dissipated was applied from 1.5-18 nW in small steps of 1.5 □ 3 nW. The inset in Fig. S2a plots the measured temperature rise at these dissipated powers, showing the temperature measurement noise floor to be ~30 µK corresponding to a power dissipation of ~7.6 nW. Hence, the temperature resolution and the heat power resolution of this calorimeter are ~30 µK and ~7.6 nW, respectively with a buffer flow rate of 4 µl/min. To validate this further, we applied DC power dissipation in steps of 7.6 nW and could clearly resolve the resulting steps of ~30 µK in the temperature rise (Fig. S3b). Further, we also measured the temperature resolution and the heat power resolution when there is no buffer flow and measured them to be ~9.5 µK and ~2 nW, respectively (Fig. S5b). While the *Drosophila* brains and tissues studied here need a buffer flow of 4 µl/min for which the heat power resolution is ~7.6 nW, this calorimeter can offer a higher sensitivity: up to ~2 nW with no buffer flow. This outlines the ultimate heat sensing capabilities of the developed calorimeter, which can be exploited when employing it for studying metabolic activity in biological samples requiring lower buffer flow rates during measurements. All above measurements are performed at a ~16 mHz bandwidth.

Fly husbandry

Adult male and female *Drosophila melanogaster* were entrained under standard 12-hour/12-hour light/dark (LD) cycles at 25°C and 50% relative humidity for a minimum of 3 days prior to

dissection. The experiments were conducted at the same time every day to control for the time-of-day variations. The flies used in the study, *y sc v*, w^{1118}, $park^{1}$, and $park^{1}/+$ were obtained from the Bloomington Drosophila Stock Center.

Dissection and culture of *Drosophila* brain explants and other tissues

Flies were anesthetized on ice for 5 □ 10 seconds before dissection. Dissections were performed in a sterile petri dish containing an ice-cold modified culture medium (buffer) adapted from the work by Ayaz et al.[32], consisting of Schneider's Drosophila Medium (Invitrogen, Carlsbad, CA) supplemented with 1% Antibiotic-Antimycotic solution (Invitrogen), 10% fetal bovine serum (FBS), and 10 μg/ml insulin. Prior studies have confirmed that these brain cultures maintain identifiable morphological features and neuronal functionality for up to 6 days[33]. Whole brains, including intact optic lobes, were carefully dissected, with cuticles and trachea removed. Testes and ovaries were similarly dissected in the same ice-cold culture medium, ensuring removal of extraneous tissues as needed. Dissected brains and tissues were rinsed three times in the medium before loading into the calorimeter, which was filled with the same buffer medium at room temperature for the calorimetric measurements. For specific experiments involving mitochondrial inhibition in brains, the following pharmacological agents were added to the culture medium: rotenone (0.5 μM), and antimycin A (0.5 μM and 20 μM).

Estimation of brain dry mass by imaging

For comparing the mass-specific metabolic outputs of the brains measured in the studies described in this paper, it was challenging and unfeasible to directly measure the dry mass of each individual brain whose metabolic activity was quantified. Hence, we estimated the mass of the brains by imaging the brains and measuring their largest area of cross-section. The traced area of cross-section of a brain is shown in Supplementary Fig. S6a. The dry mass of a brain is

directly proportional to its volume, which can be approximated as the 1.5^{th} power of the cross-sectional area, assuming an isometric scaling. To estimate the proportionality constant relating brain volume to the dry mass, we simultaneously measured the dry mass and the cross-sectional area for 6 female brains of 10-day-old Drosophila flies (*y sc v* genotype). The proportionality constant was estimated to be ~26.3 μg/mm^3 by plotting the dry masses against the 1.5^{th} power of the cross-sectional area measured for these 6 brains (shown in Supplementary Fig. S6b).

Dry mass measurements using ultra-microbalance

A Mettler Toledo XP2U ultra-microbalance (resolution: 0.2 μg) was used for measuring the dry mass of brains, ovaries, and testes. Supplementary Fig. S7a shows the followed procedure. Weighing boats (~1 mm × 1 mm in size) were prepared out of aluminum foil and their masses were measured with the microbalance. The average mass of an empty boat was ~100 μg. For dry mass measurement, a tissue was first dissected in the buffer medium. Next, it was quickly rinsed (for 2 □ 3 seconds) in de-ionized (DI) water to get rid of the buffer salts and then transferred to a boat. The boat with the tissue was transferred to a temperature-controlled chamber (TestEquity Model TEC1) and heated at 50°C for 5 hours to dehydrate the tissue. Finally, the dry mass of the tissue in the boat was measured using the microbalance and the pre-calibrated mass of the boat was subtracted to obtain the tissue dry mass. Supplementary Fig. S7b plots the measured dry masses of several female brains, ovaries, and testes from 10-day-old *Drosophila* flies (*y sc v* genotype).

Data analysis

Basal metabolic rate was calculated for an individual fly brain or tissue by averaging its heat output over ~30 minutes of stable measurement, as shown in the individual measurement traces in Fig. 1c and Supplementary Fig. S8. Statistical analysis to compare the effects of inhibitors,

gender, genotype, age, and disease on metabolic rates, was performed using the two-tailed *t* test in OriginPro 2022 and computing the *p*-values. In the data shown, $p \leq 0.0001$, $p \leq 0.001$, $p \leq 0.01$, and $p \leq 0.05$ are indicated by □□□□, □□□, □□, and □, respectively. A *p*-value > 0.05 suggests there is no significant (ns) difference between data sets.

Acknowledgements

We thank the members of the Reddy, Meyhofer, and Yadlapalli laboratories for helpful discussions. We thank the Bloomington Drosophila Stock Center (P40 OD018537) for providing fly strains. This work was supported by National Institutes of Health NIGMS R35GM133737 grant to S.Y., the Alfred P. Sloan fellowship, the McKnight scholar grant, and the Chan Zuckerberg collaborative pairs grant to S.Y.

Author Contributions

P.R., E.M., and S.Y. conceived the work. K. P. and R.M. developed the instrument. K.P. performed all calorimetric experiments. R.M. assisted with preliminary calorimetric experiments. K.P. and A.B. performed all dry mass measurements. Q. C. and S. Y performed fly husbandry and all dissections. The manuscript was written by K.P., P.R., E.M., and S.Y. with comments and input from all authors.

Corresponding author

Correspondence to Pramod Reddy, Edgar Meyhofer, and Swathi Yadlapalli.

Conflicts of interest

The authors declare no financial conflict of interest.

References

1. Raichle, M.E. & Gusnard, D.A. Appraising the brain's energy budget. *Proc Natl Acad Sci U S A* **99**, 10237-10239 (2002).
2. Butterfield, D.A. & Halliwell, B. Oxidative stress, dysfunctional glucose metabolism and Alzheimer disease. *Nat Rev Neurosci* **20**, 148-160 (2019).
3. Gao, G., Shi, Y., Deng, H.X. & Krainc, D. Dysregulation of mitochondrial alpha-ketoglutarate dehydrogenase leads to elevated lipid peroxidation in CHCHD2-linked Parkinson's disease models. *Nat Commun* **16**, 1982 (2025).
4. Mattson, M.P. & Arumugam, T.V. Hallmarks of Brain Aging: Adaptive and Pathological Modification by Metabolic States. *Cell Metab* **27**, 1176-1199 (2018).
5. Hou, Y.J. et al. Ageing as a risk factor for neurodegenerative disease. *Nat Rev Neurol* **15**, 565-581 (2019).
6. Clish, C.B. Metabolomics: an emerging but powerful tool for precision medicine. *Cold Spring Harb Mol Case Stud* **1**, a000588 (2015).
7. Fessenden, M. Metabolomics: Small Molecules, Single Cells. *Nature* **540**, 153-155 (2016).
8. Hollywood, K., Brison, D.R. & Goodacre, R. Metabolomics: current technologies and future trends. *Proteomics* **6**, 4716-4723 (2006).
9. Liu, X. & Locasale, J.W. Metabolomics: A Primer. *Trends Biochem Sci* **42**, 274-284 (2017).
10. Wishart, D.S. Metabolomics for Investigating Physiological and Pathophysiological Processes. *Physiol Rev* **99**, 1819-1875 (2019).
11. Wishart, D.S. NMR metabolomics: A look ahead. *J Magn Reson* **306**, 155-161 (2019).
12. Hütter, E., Unterluggauer, H., Garedew, A., Jansen-Dürr, P. & Gnaiger, E. High-resolution respirometry -: a modern tool in aging research. *Exp Gerontol* **41**, 103-109 (2006).
13. Ota, A., Ishihara, T. & Ishihara, N. Mitochondrial nucleoid morphology and respiratory function are altered in Drp1-deficient HeLa cells. *J Biochem* **167**, 287-294 (2020).
14. Kuznetsov, A.V. et al. Analysis of mitochondrial function in situ in permeabilized muscle fibers, tissues and cells. *Nat Protoc* **3**, 965-976 (2008).
15. Kenny, G.P., Notley, S.R. & Gagnon, D. Direct calorimetry: a brief historical review of its use in the study of human metabolism and thermoregulation. *Eur J Appl Physiol* **117**, 1765-1785 (2017).
16. Kaiyala, K.J. & Ramsay, D.S. Direct animal calorimetry, the underused gold standard for quantifying the fire of life. *Comp Biochem Physiol A Mol Integr Physiol* **158**, 252-264 (2011).
17. Voet, D. & Voet, J.G. Biochemistry, Edn. 4th. (John Wiley & Sons, Hoboken, NJ; 2011).
18. Alberts, B., Wilson, J.H. & Hunt, T. Molecular biology of the cell, Edn. 5th. (Garland Science, New York; 2008).
19. Rodenfels, J., Neugebauer, K.M. & Howard, J. Heat Oscillations Driven by the Embryonic Cell Cycle Reveal the Energetic Costs of Signaling. *Dev Cell* **48**, 646-658 e646 (2019).
20. Rodenfels, J., Neugebauer, K.M. & Howard, J. Heat Oscillations Driven by the Embryonic Cell Cycle Reveal the Energetic Costs of Signaling. *Dev Cell* **53**, 492 (2020).
21. Rodenfels, J. et al. Contribution of increasing plasma membrane to the energetic cost of early zebrafish embryogenesis. *Mol Biol Cell* **31**, 520-526 (2020).

22. Foster, P.J., Razo-Mejia, M. & Phillips, R. Measuring the Energetic Costs of Embryonic Development. *Developmental Cell* **48**, 591-592 (2019).
23. Fiorino, A. et al. Parallelized, real-time, metabolic-rate measurements from individual. *Sci Rep-Uk* **8** (2018).
24. Hur, S., Mittapally, R., Yadlapalli, S., Reddy, P. & Meyhofer, E. Sub-nanowatt resolution direct calorimetry for probing real-time metabolic activity of individual C. elegans worms. *Nat Commun* **11**, 2983 (2020).
25. Hong, S. et al. Sub-nanowatt microfluidic single-cell calorimetry. *Nat Commun* **11**, 2982 (2020).
26. Liao, D., Hessler, N.A. & Malinow, R. Activation of postsynaptically silent synapses during pairing-induced LTP in CA1 region of hippocampal slice. *Nature* **375**, 400-404 (1995).
27. Delpech, C. et al. Axon guidance during mouse central nervous system regeneration is required for specific brain innervation. *Dev Cell* **59**, 3213-3228 e3218 (2024).
28. Incropera, F.P., DeWitt, D.P., Bergman, T.L. & Lavine, A.S. Fundamentals of heat and mass transfer, Vol. 6. (Wiley New York, 1996).
29. Zheng, Z. et al. A Complete Electron Microscopy Volume of the Brain of Adult Drosophila melanogaster. *Cell* **174**, 730-743 e722 (2018).
30. Panda, K., Mittapally, R., Reddy, P., Yadlapalli, S. & Meyhofer, E. Micro-kelvin temperature-stable system for biocalorimetry applications. *Rev Sci Instrum* **95** (2024).
31. Sadat, S., Meyhofer, E. & Reddy, P. Resistance thermometry-based picowatt-resolution heat-flow calorimeter. *Applied Physics Letters* **102**, 163110 (2013).
32. Ayaz, D. et al. Axonal injury and regeneration in the adult brain of Drosophila. *J Neurosci* **28**, 6010-6021 (2008).
33. Roberts, L. et al. Light evokes rapid circadian network oscillator desynchrony followed by gradual phase retuning of synchrony. *Curr Biol* **25**, 858-867 (2015).
34. Gnaiger, E., Mendez, G. & Hand, S.C. High phosphorylation efficiency and depression of uncoupled respiration in mitochondria under hypoxia. *Proc Natl Acad Sci U S A* **97**, 11080-11085 (2000).
35. Diaz-Cuadros, M. et al. Metabolic regulation of species-specific developmental rates. *Nature* **613**, 550-557 (2023).
36. Diaz-Cuadros, M. et al. Metabolic regulation of species-specific developmental rates (Jan, 10.1038/s41586-022-05574-4, 2023). *Nature* **616**, E4-E4 (2023).
37. Narendra, D., Tanaka, A., Suen, D.F. & Youle, R.J. Parkin is recruited selectively to impaired mitochondria and promotes their autophagy. *J Cell Biol* **183**, 795-803 (2008).
38. Pickrell, A.M. & Youle, R.J. The roles of PINK1, parkin, and mitochondrial fidelity in Parkinson's disease. *Neuron* **85**, 257-273 (2015).
39. Clark, I.E. et al. Drosophila pink1 is required for mitochondrial function and interacts genetically with parkin. *Nature* **441**, 1162-1166 (2006).
40. Li, H. et al. Fly Cell Atlas: A single-nucleus transcriptomic atlas of the adult fruit fly. *Science* **375**, eabk2432 (2022).
41. Lee, W., Fon, W., Axelrod, B.W. & Roukes, M.L. High-sensitivity microfluidic calorimeters for biological and chemical applications. *Proc Natl Acad Sci U S A* **106**, 15225-15230 (2009).
42. Sadat, S., Meyhofer, E. & Reddy, P. High resolution resistive thermometry for micro/nanoscale measurements. *Rev Sci Instrum* **83**, 084902 (2012).

43. Skogestad, S. in AIChE Annual Meeting (Reno, NV, USA; 2001).

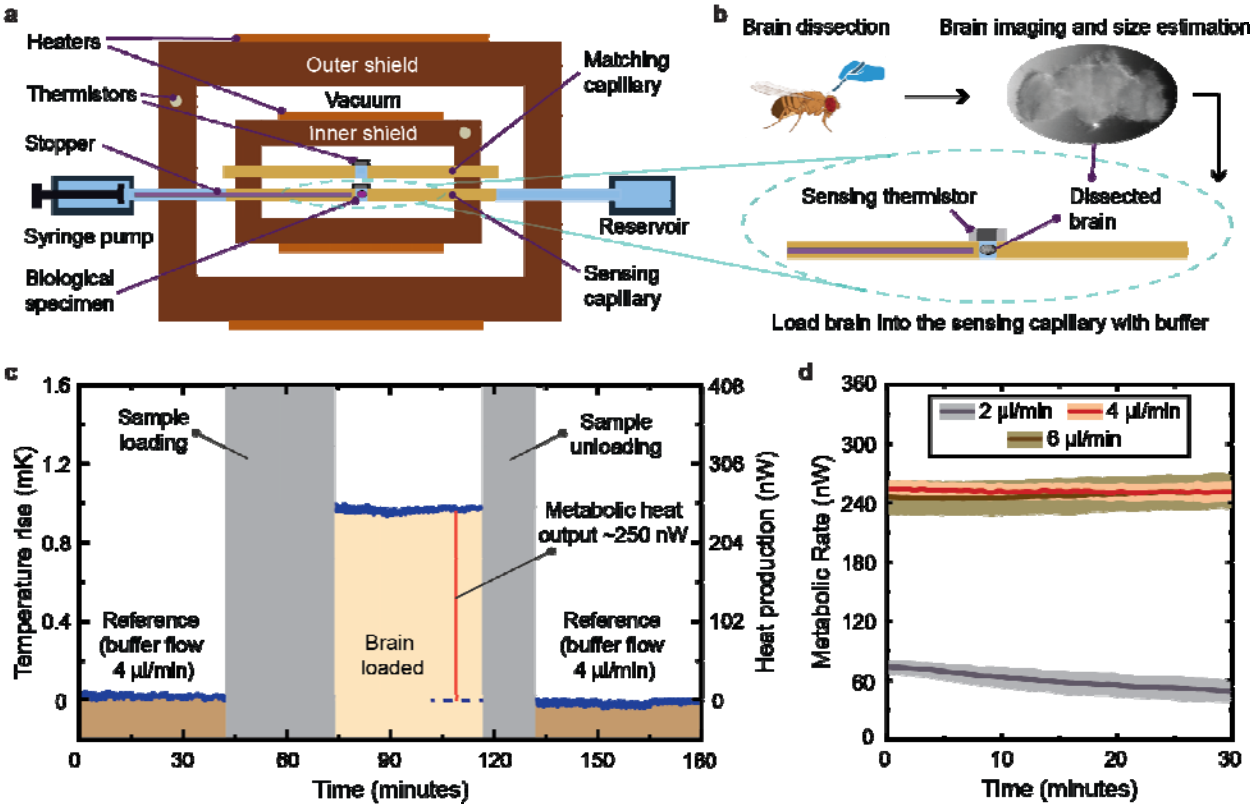

Fig. 1: **Method for measuring metabolic output in *Drosophila* brains** (a) A schematic top view of the high-resolution biocalorimeter with the thermal shields, the sensing and matching capillary tubes, the syringe pump and the fluid reservoir. The two nested shields, along with ultra-high vacuum and precision electronics, are used to maintain high-temperature stability in the system. The sensing capillary is used for metabolic measurements, and the matching capillary is employed for common-mode cancellation of ambient temperature drifts. The syringe pump and the reservoir help maintain a continuous flow of a physiological buffer to keep the biological specimen alive during measurements. (b) For metabolic output measurements, the brain is dissected from a *Drosophila* fly, imaged for dry mass estimation, and then loaded into the sensing capillary filled with the buffer. The brain is located near the sensing thermistor by the stopper and the measurement begins. (c) A trace of the metabolic rate measurement of a brain from a 10-day-old female fruit fly (*y sc v* genotype) with a buffer flow rate of 4 µl/min. The reference temperature is recorded before the measurement. Once the brain is loaded near the thermistor, the metabolic output from the brain raises the temperature in its vicinity, which is recorded by the sensing thermistor. Loading the brain perturbs the system, which takes ~20 minutes to stabilize. Following stabilization, the measurement is performed for 30 □ 40 minutes, after which the brain is unloaded, and the reference signal is recorded again. The difference in the temperature signal when the brain is in and out of the sensing capillary gives an estimate of the metabolic output of the brain. (d) The optimum buffer flow rate is determined to be 4 µl/min for measuring the metabolic activity of *Drosophila* brains. Metabolic output measurements were

performed with several brains (10-day-old, female flies, *y sc v* genotype) at buffer flow rates of 2 µl/min, 4 µl/min, and 6 µl/min. The plot shows the mean (solid line) and the standard error of mean (lighter shaded region) of all measured traces over 30 minutes of measurement at these flow rates.

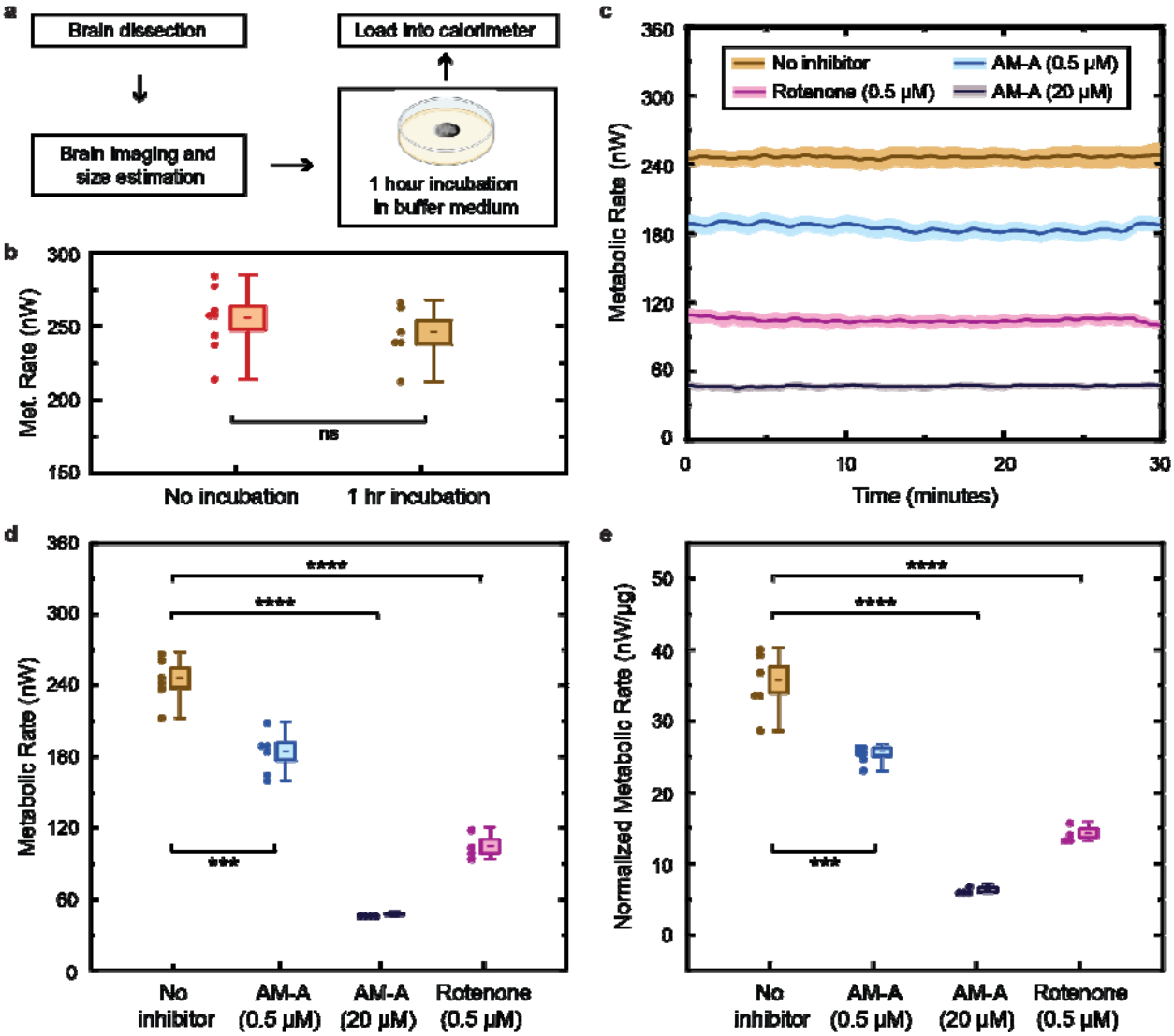

Fig. 2: Effect of mitochondrial inhibitors on brain metabolism (a) The method followed for these measurements include a 1-hour incubation time in the buffer-inhibitor media after imaging and before loading the brains into the calorimeter for measurement. (b) Control experiments were performed to show that the additional 1-hour incubation time has no effect on the metabolic rate of brains measured with the control buffer without any inhibitor. (c) The averaged metabolic rate traces of the brains in buffer without any inhibitor, with antimycin-A (AM-A) at 0.5 µM and 20 µM concentrations, and with rotenone at 0.5 µM concentration are plotted, showing the mean (solid line) and the standard error of mean (SEM, lighter shaded region). (d) Distribution of the absolute metabolic rates of the brains with the above inhibitors is plotted. A suppression in metabolic rates is observed due to the inhibitors. (e) Distribution of the normalized metabolic rates of the brains with the inhibitors is shown, which follows a similar trend. The distribution

plots show the individual data points (solid circles), the mean (dash), the SEM (shaded box), and the maximum and minimum values (whiskers). A *p*-value > 0.05 suggests there is no significant (ns) difference between data sets, and □□□□, □□□, □□, and □, indicate *p*□≤□0.0001, *p*□≤□0.001, $p \leq 0.01$, and $p \leq 0.05$, respectively.

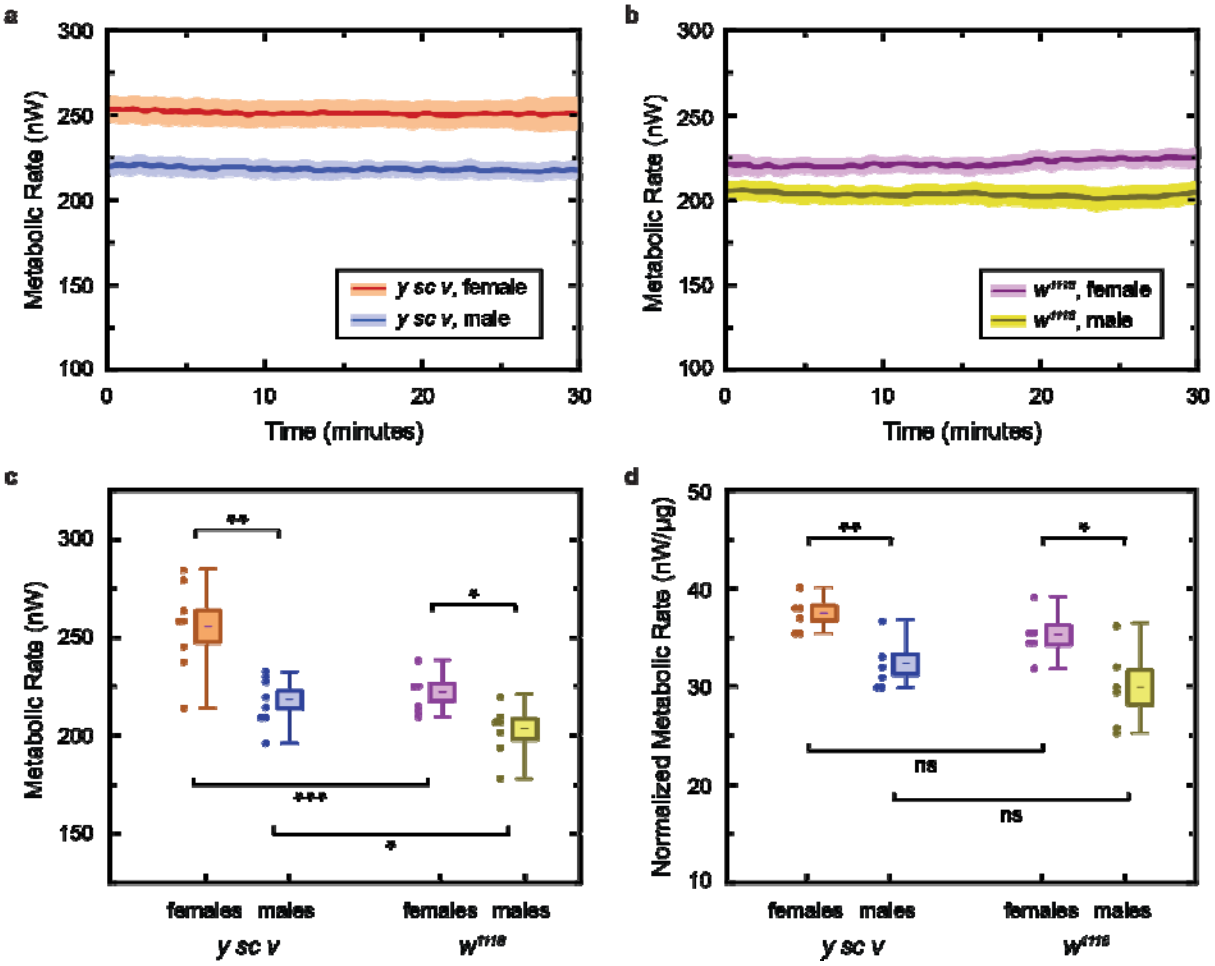

Fig. 3: Metabolic activity in fly brains across different genders and genotypes (a) Averaged metabolic output as a function of time is shown for female and male brains of 10-day-old flies from the *y sc v* and (b) w^{1118} genotypes. The mean (solid line) and the standard error of mean (SEM, lighter shaded region) are shown. (c) Distribution of absolute metabolic rates of the measured brains is plotted. In both genotypes, females show a higher absolute metabolic rate than males. Both genders of the *y sc v* genotype show a higher absolute metabolic rate compared to the respective genders of the w^{1118} genotype. (d) Distribution of normalized metabolic rates of the measured brains is shown. In both genotypes, females show a higher normalized metabolic rate than males. However, there is no significant difference between the normalized metabolic rates of the same gender across the two genotypes. The distribution plots show each measured data point (solid circles), the mean (dash), the SEM (shaded box), and the maximum and minimum values (whiskers). A *p*-value > 0.05 suggests there is no significant (ns) difference between data sets, and □□□□, □□□, □□, and □, indicate *p*□≤□0.0001, *p*□≤□0.001, $p \leq 0.01$, and $p \leq 0.05$, respectively.

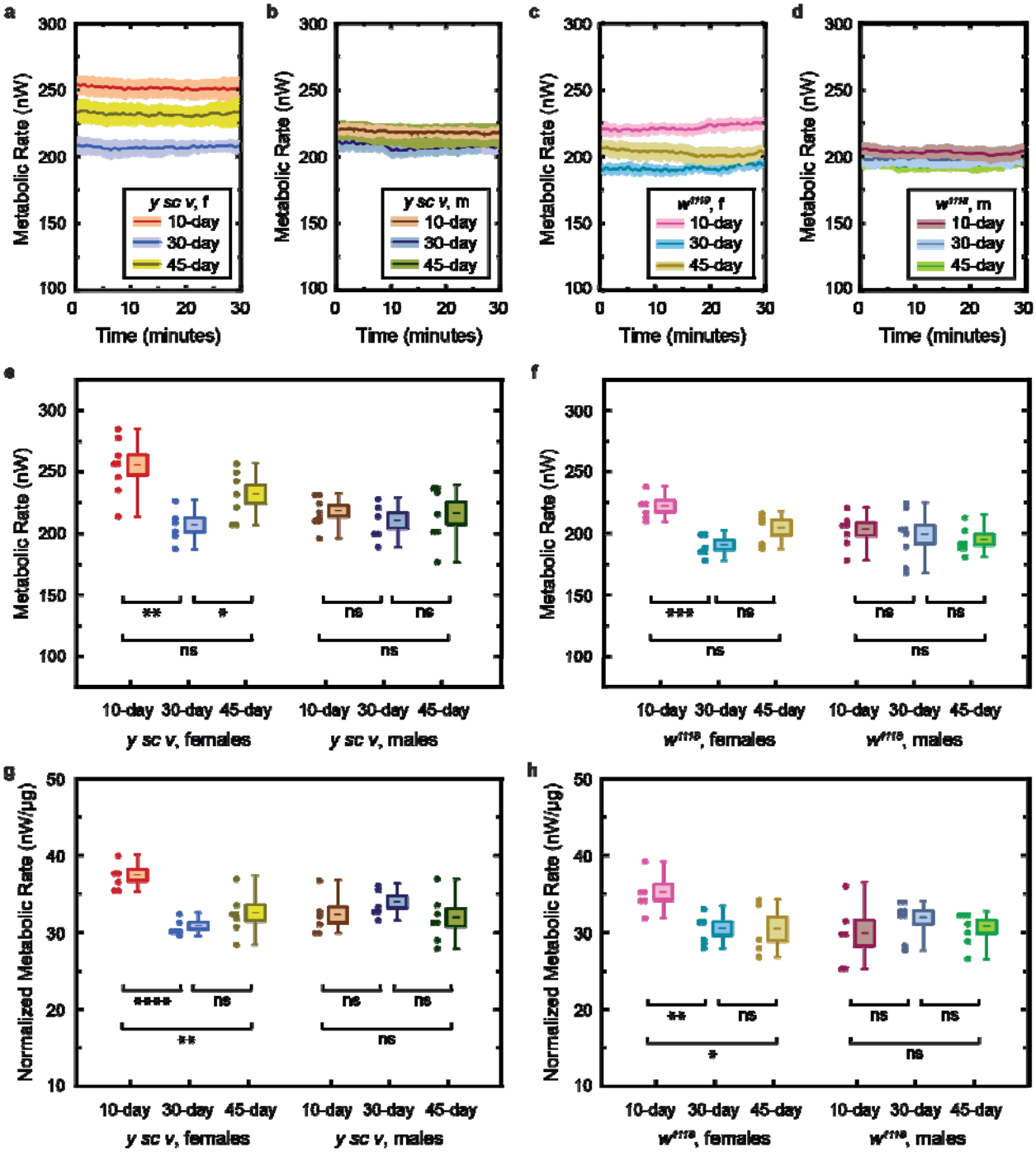

Fig. 4: Metabolic activity in fly brains across lifespan (a) Averaged absolute metabolic output as a function of time is shown for brains of 10-, 30- and 45-day-old female flies of the *y sc v* genotype (*y sc v*, f), (b) male flies of the *y sc v* genotype (*y sc v*, m), (c) female flies of the w^{1118} genotype (w^{1118}, f) and (d) male flies of the w^{1118} genotype (w^{1118}, m). The mean (solid line) and the standard error of mean (SEM, lighter shaded region) are shown. (e) Distribution of absolute metabolic rates of the measured brains from female and male flies of the *y sc v* and (f) w^{1118} genotypes. The absolute metabolic rates of the female brains sharply reduce from age day-10 to day-30, and then slightly increase or remain constant from day-30 to day-45, depending on the

genotype. In contrast, the absolute metabolic rates of the male brains remain constant throughout their lifespan, in both the genotypes. (g) Distribution of normalized metabolic rates of the measured brains from female and male flies of the *y sc v* and (h) w^{1118} genotypes. In both genotypes, the normalized metabolic rates of the female brains are higher at day-10 compared to day-30 or day-45, while the normalized metabolism in males remained constant throughout their lifespan. The distribution plots show each measured data point (solid circles), the mean (dash), the SEM (shaded box), and the maximum and minimum values (whiskers). A *p*-value > 0.05 suggests there is no significant (ns) difference between data sets, and □□□□, □□□, □□, and □, indicate p□≤□0.0001, p□≤□0.001, $p \leq 0.01$, and $p \leq 0.05$, respectively.

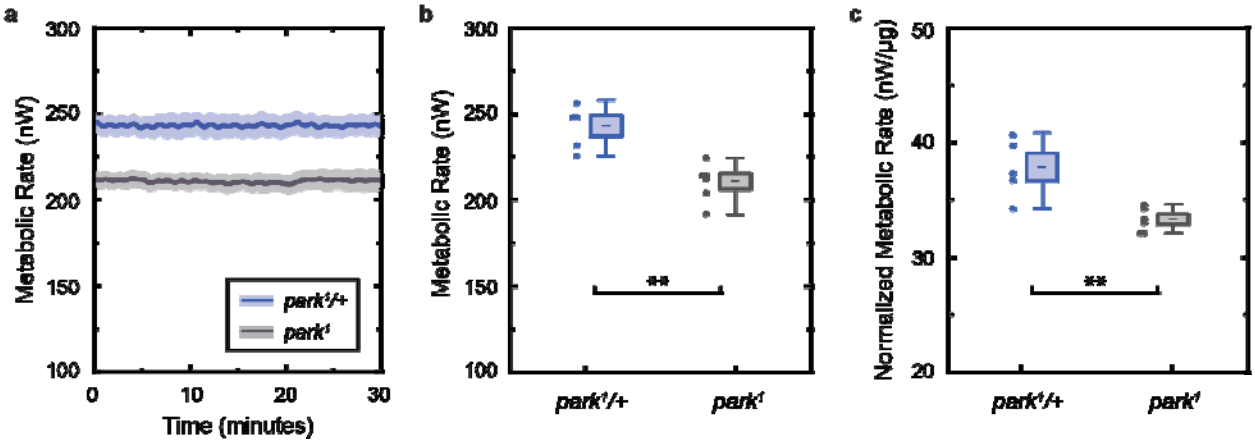

Fig. 5: Metabolic activity in brains of mitochondrial mutant flies (a) Averaged absolute metabolic output as a function of time is plotted for heterozygous (*park*^{1}/+) and homozygous (*park*^{1}) mutant fly brains. The mean (solid line) and the standard error of mean (SEM, lighter shaded region) are shown. (b) Distribution of the absolute metabolic rates is plotted, showing a ~15% suppression in the metabolism of homozygous fly brains compared to heterozygous brains. (c) Distribution of the normalized metabolic rates also shows a similar reduction in metabolism of the homozygous mutant brains. The distribution plots show each measured data point (solid circles), the mean (dash), the SEM (shaded box), and the maximum and minimum values (whiskers). A *p*-value > 0.05 suggests there is no significant (ns) difference between data sets, and □□□□, □□□, □□, and □, indicate *p*□≤□0.0001, *p*□≤□0.001, $p \leq 0.01$, and $p \leq 0.05$, respectively.

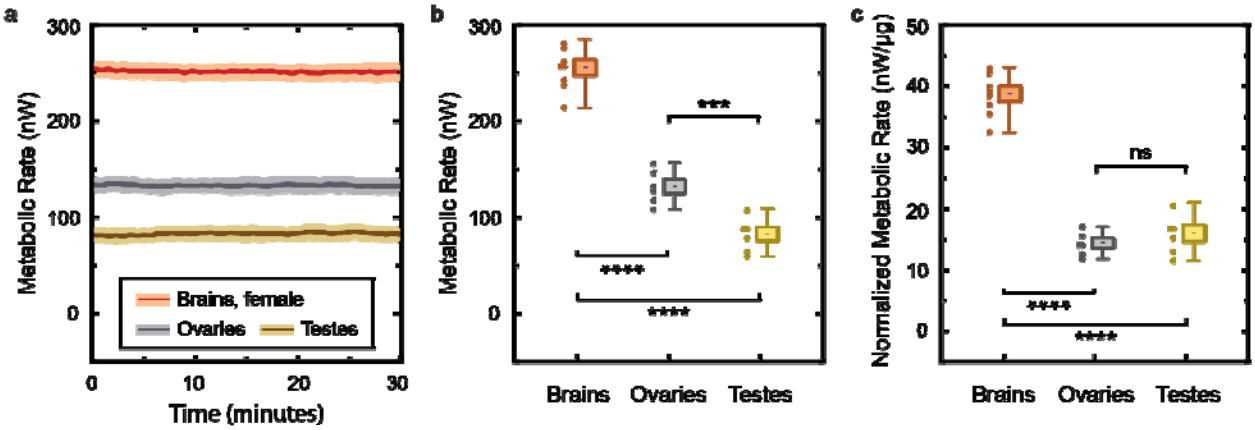

Fig. 6: Metabolic activity in other *Drosophila* tissues (a) Averaged absolute metabolic output as a function of time for female brains, ovaries, and testes of 10-day-old flies (*y sc v* genotype). The mean (solid line) and the standard error of mean (SEM, lighter shaded region) are shown. (b) Distribution of the absolute metabolic rates of the measured tissues. The mean metabolic output of the female brains, ovaries, and testes were ~256 nW, ~132 nW, and ~83 nW, respectively. (c) Distribution of normalized metabolic rates of the brains, ovaries and testes. The mean of the normalized metabolic outputs of the female brains, ovaries, and testes were ~38.7 nW/µg, ~14.4 nW/µg, and 15.9 nW/µg, respectively. The normalized metabolic outputs of the ovaries and the testes are similar (~15 nW/µg), while that of the brains is ~2.5-fold higher, showing the brain is more energy-consuming than the reproductive organs in *Drosophila*. The distribution plots show each measured data point (solid circles), the mean (dash), the SEM (shaded box), and the maximum and minimum values (whiskers). A *p*-value > 0.05 suggests there is no significant (ns) difference between data sets, and □□□□, □□□, □□, and □, indicate *p*□≤□0.0001, *p*□≤□0.001, $p \leq 0.01$, and $p \leq 0.05$, respectively.